Supporting Information

General Oriented Formation of Carbon Nanotubes from Metal-Organic Frameworks

Jiashen Meng, [1,†] Chaojiang Niu, [1,†] Linhan Xu, [2,†] Jiantao Li, [1] Xiong Liu,[1] Xuanpeng Wang, [1] Yuzhu Wu, [1] Xiaoming Xu, [1] Wenyi Chen, [1] Qi Li, [1] Zizhong Zhu, [2,]* Dongyuan Zhao, [1] Liqiang Mai[1,3]*

[1]State Key Laboratory of Advanced Technology for Materials Synthesis and Processing, Wuhan University of Technology, Wuhan 430070, China

[2]Department of Physics and Collaborative Innovation Center for Optoelectronic Semiconductors and Efficient Devices, Xiamen University, Xiamen 361005, China

[3]Department of Chemistry, University of California, Berkeley, California 94720, United States

[†]These authors contributed equally to this work.

E-mail: mlq518@whut.edu.cn; zzhu@xmu.edu.cn

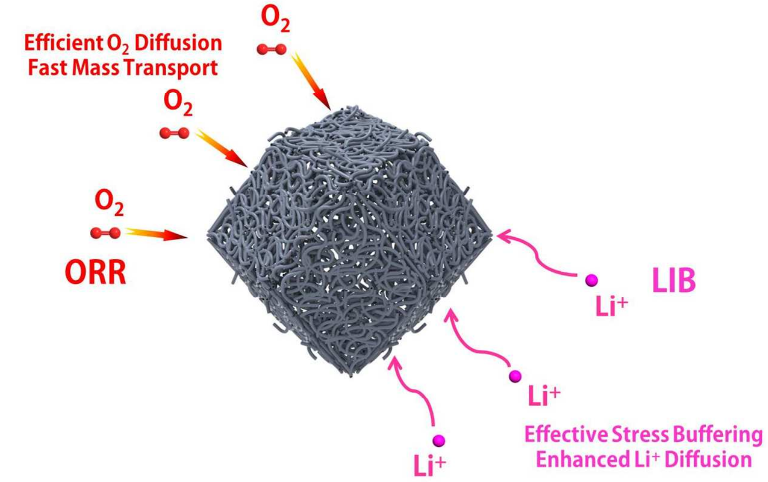

Figure S1. Schematic illustration of N-CNT-assembled hollow dodecahedra for ORR and LIB. This architecture can possess efficient O_2 diffusion and fast mass transport in ORR. And this architecture can provide effective stress buffering and enhanced Li^+ diffusion in LIB.

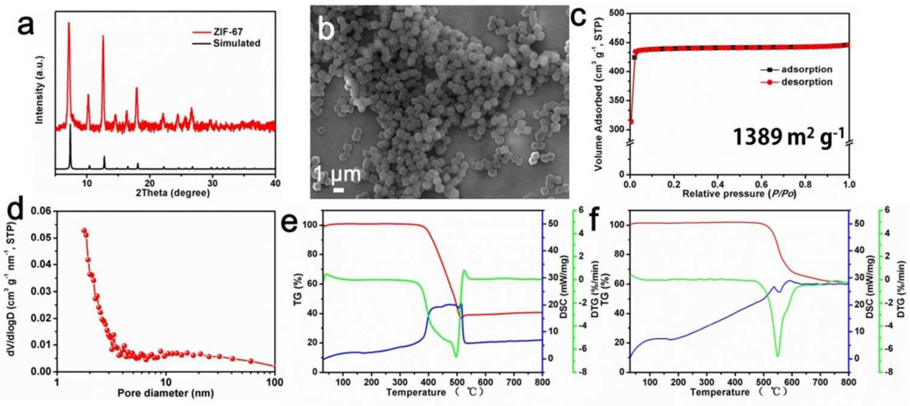

Figure S2. Characterizations of ZIF-67 dodecahedra. (a) XRD of ZIF-67 dodecahedra and a comparison with experimental and simulated XRD patterns of ZIF-67. (b) SEM image of ZIF-67 dodecahedra. (c, d)N_2 adsorption-desorption isotherms and the pore size distribution of ZIF-67 dodecahedra, respectively. (e, f) TG-DTG-DSC curves of ZIF-67 dodecahedra in air and argon, respectively.

The nitrogen adsorption-desorption isotherm of ZIF-67 shows a high BET specific surface area of 1389 m^2 g^{-1}, and the typical type I Langmuir isotherm indicates the microporous structure.

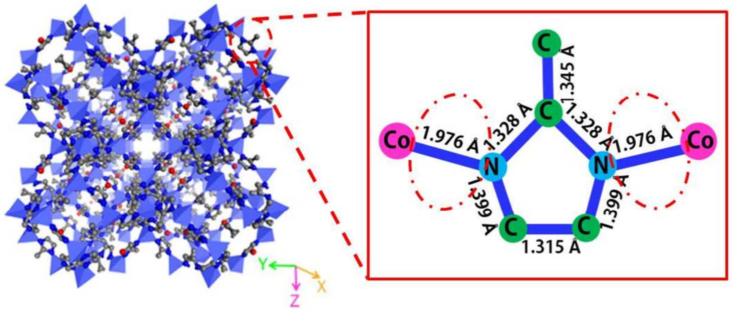

Figure S3. Detailed crystal parameters of ZIF-67. The crystal parameters show that the Co-N bonds have larger bond length than others, indicating preferential bond breaking.

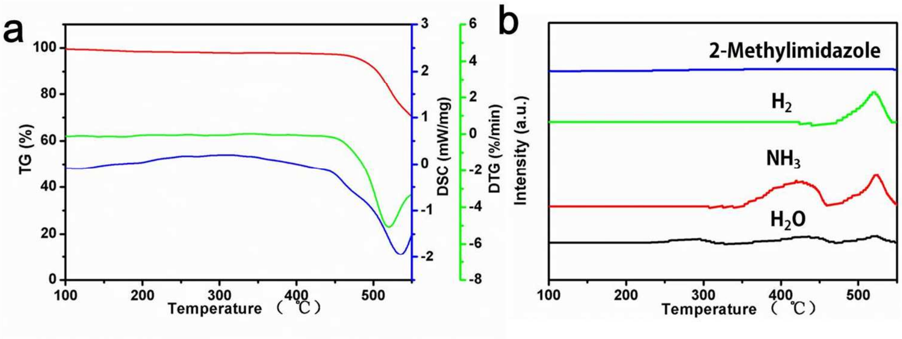

Figure S4. Characterizations of the pyrolysis process of ZIF-67 dodecahedra by TGA-MS technique. (a) TG, DSC and DTG curves of ZIF-67 dodecahedra. (b) the corresponding MS curves of 2-methylimidazole, H_2, NH_3 and H_2O, respectively.

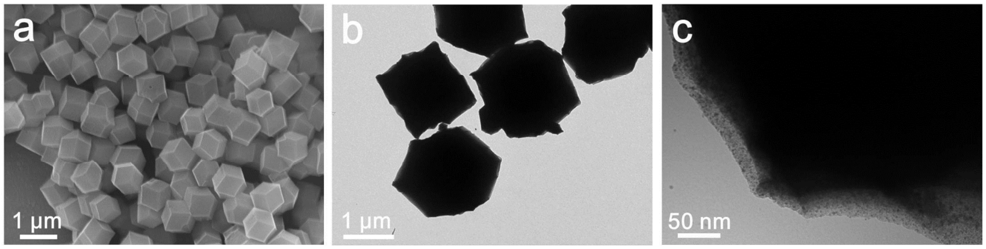

Figure S5. Characterizations of the sample prepared for 0.5 h. (a) SEM image. (b, c) TEM images.

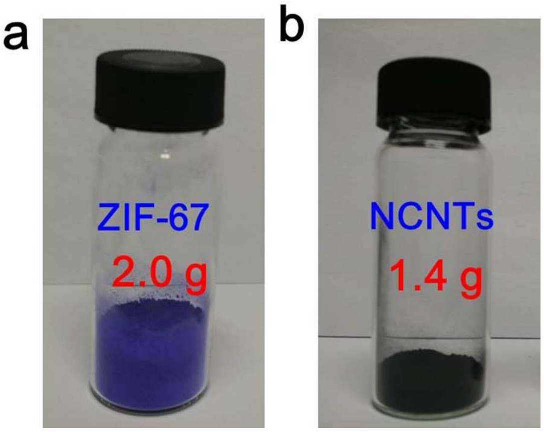

Figure S6. Yield evaluations of N-CNTs from ZIF-67. (a) Digital photo shows 2.0 g of ZIF-67 dodecahedron precursor before pyrolysis. (b) Digital photo shows 1.4 g of ZIF-67 dodecahedra-derived N-CNTs after full pyrolysis at 435 °C for 8 h in argon.

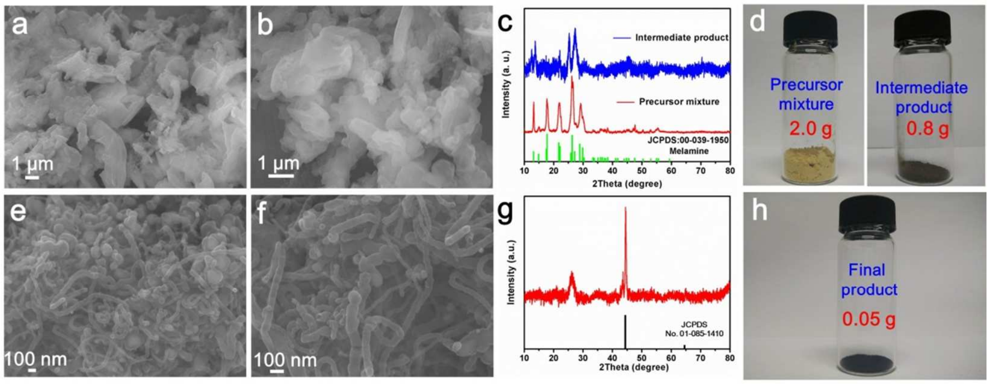

Figure S7. Characterizations of the synthesis process of N-CNTs via traditional solid-phase method. (a) SEM image of the precursor mixture. (b) SEM image of the intermediate product after treated at at 435 °C (2 °C min^{-1}) in argon for 8 h. (c) The corresponding XRD patterns of the precursor mixture and intermediate product. (d) Digital photo shows 2.0 g of the precursor mixture before pyrolysis and 0.8 g of intermediate product. (e, f) SEM image of N-CNTs after treated by 900 °C (2 °C min^{-1}) in argon for 2 h. (g) The corresponding XRD pattern of N-CNTs. (h) Digital photo shows 0.05 g of the final product after treated by 900 °C (2 °C min^{-1}) in argon for 2 h.

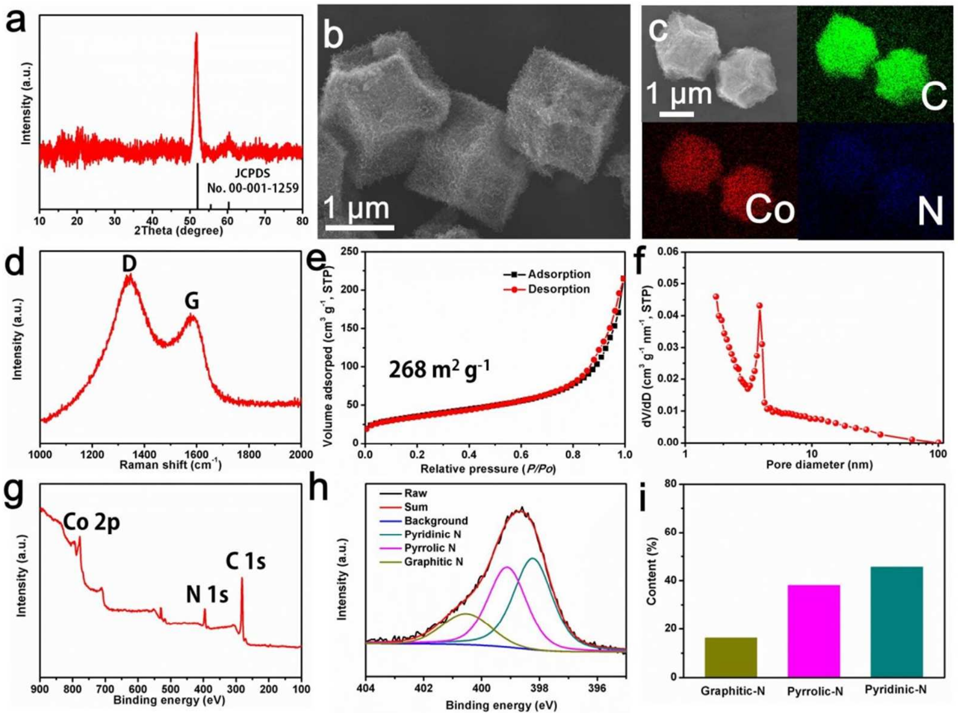

Figure S8. Characterizations of ZIF-67-derived N-CNT-assembled hollow dodecahedra. (a) XRD patterns. (b) SEM image. (c) Elemental mapping images of Co, N and C elements. (d) Raman spectrum. (e, f) N_2 adsorption-desorption isotherms and the pore size distribution. (g) XPS spectrum. (h) High resolution N 1s XPS spectrum. (i) The corresponding content of three nitrogen species.

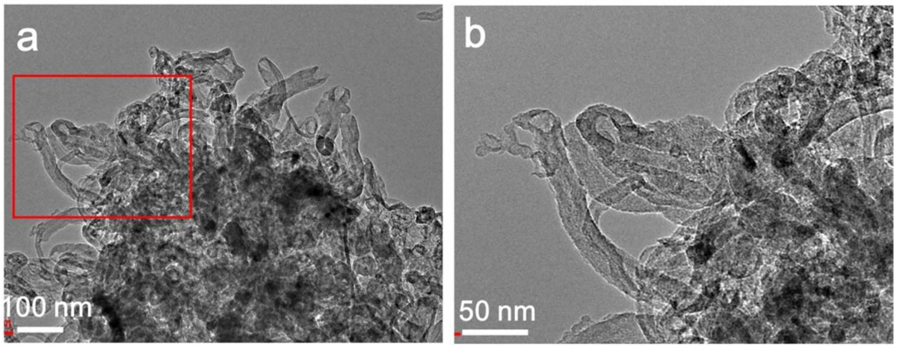

Figure S9. Morphology characterizations of ZIF-67-derived N-CNT-assembled hollow dodecahedra. (a, b) TEM images after the N-CNTs sample was washed by hydrochloric acid.

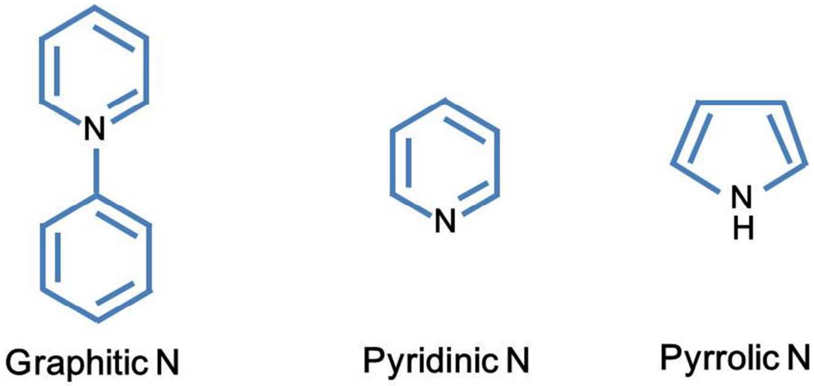

Figure S10. Structural illustrations of graphitic N, pyridinic N and pyrrolic N, respectively.

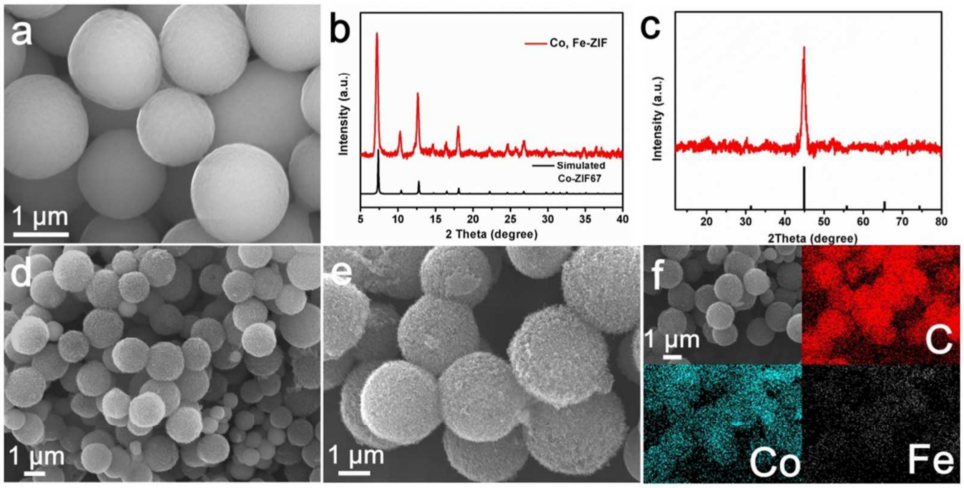

Figure S11. Characterizations of Co, Fe-ZIF precursor and derived N-CNT-assembled microspheres. (a) SEM image of Co, Fe-ZIF precursor. (b) XRD pattern of Co, Fe-ZIF precursor. (c) XRD pattern of derived N-CNT-assembled microspheres. (d, e) SEM images of derived N-CNT-assembled microspheres. (f) Elemental mapping images of derived N-CNT-assembled microspheres, including Co, C and Fe elements.

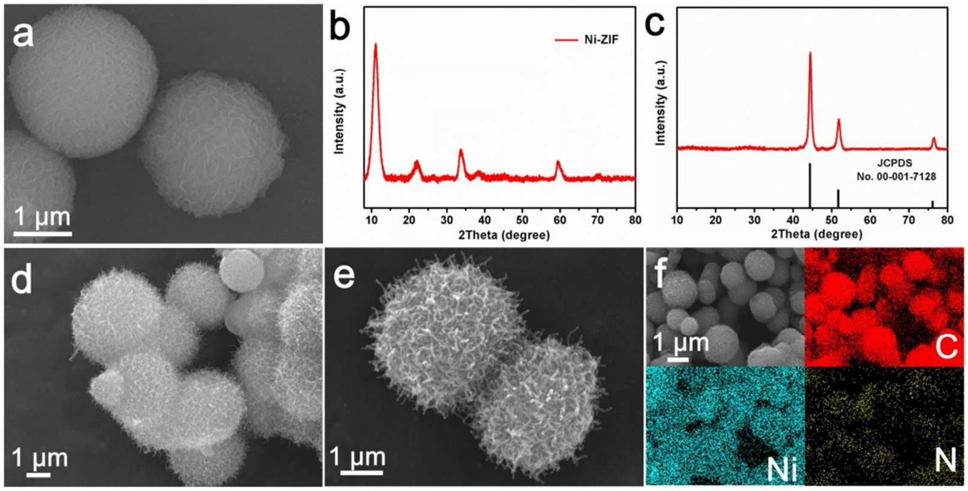

Figure S12. Characterizations of Ni-ZIF precursor and derived N-CNT-ssembled microspheres. (a) SEM image of Ni-ZIF precursor. (b) XRD pattern of Ni-ZIF precursor. (c) XRD pattern of derived N-CNT-assembled microspheres. (d, e) SEM images of derived N-CNTs assembled microspheres. (f) Elemental mapping images of derived N-CNTs assembled microspheres, including C, Ni and N elements.

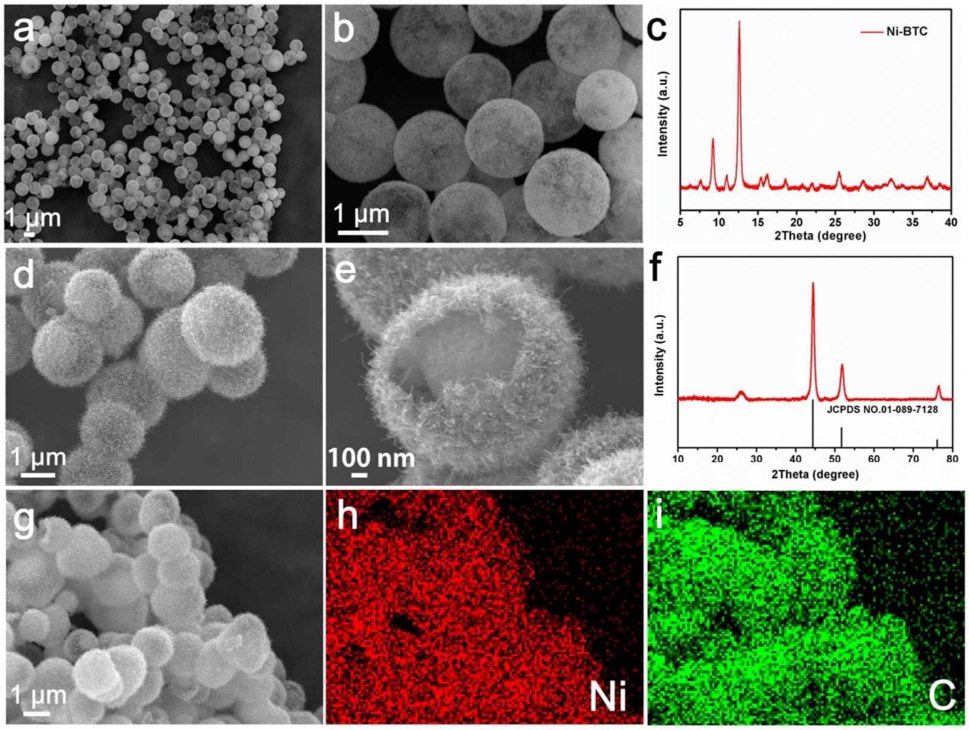

Figure S13. Characterizations of hollow Ni-BTC precursor and derived CNT-assembled hollow microspheres. (a, b) SEM imagesof hollow Ni-BTC precursor. (c) XRD pattern of hollow Ni-BTC precursor. (d, e) SEM images of derived CNT-assembled hollow microspheres. (f) XRD pattern of derived CNT-assembled hollow microspheres. (g-i) Elemental mapping images of derived CNT-assembled hollow microspheres, including Ni and C elements.

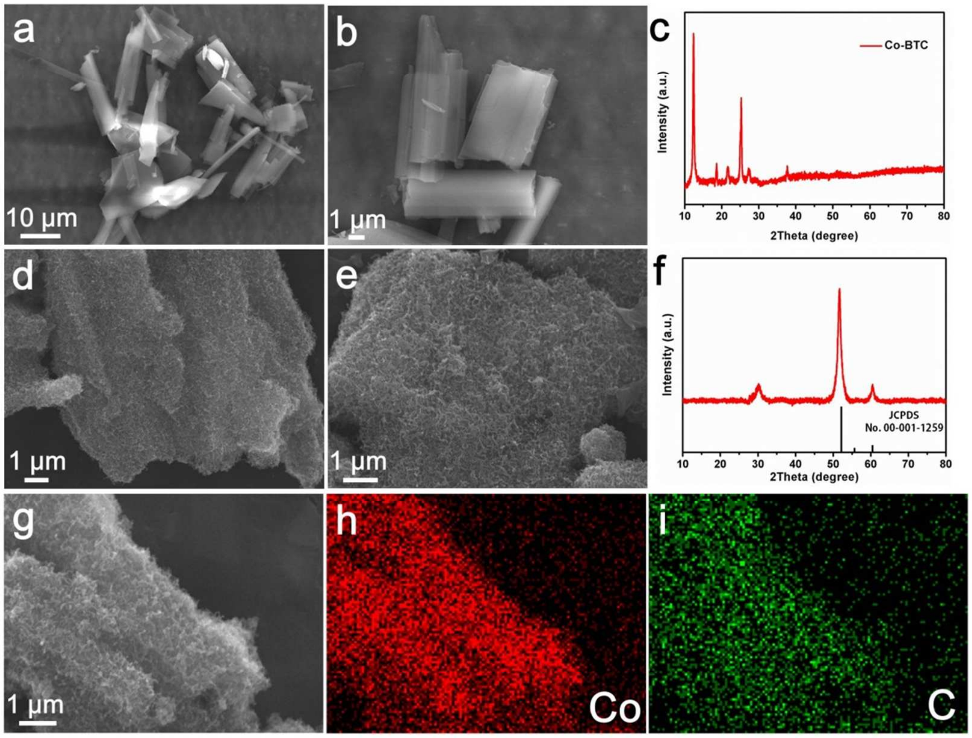

Figure S14. Characterizations of Co-BTC precursor and derived CNT-assembled microsheets. (a, b) SEM images of Co-BTC precursor. (c) XRD pattern of Co-BTC precursor. (d, e) SEM images of derived CNT-assembled microsheets. (f) XRD pattern of derived CNT-assembled microsheets. (g-i) Elemental mapping images of derived CNT-assembled microsheets, including Co and C elements.

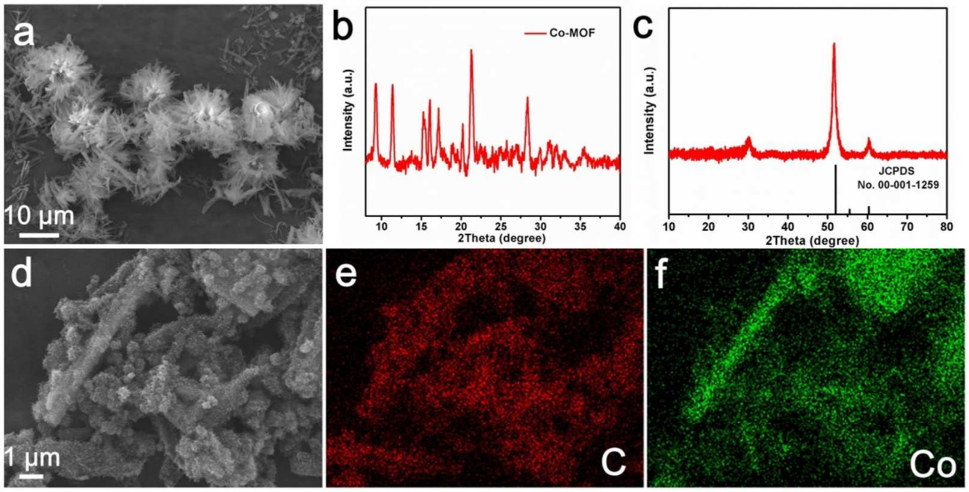

Figure S15. Characterizations of Co-MOF precursor and derived CNT-assembled nanorods. (a) SEM image of Co-MOF precursor. (b) XRD pattern of Co-MOF precursor. (c) XRD pattern of derived CNT-assembled nanorods. (d) SEM image of derived CNT-assembled nanorods. (e, f) Elemental mapping images of derived CNT-assembled nanorods, including C and Co elements.

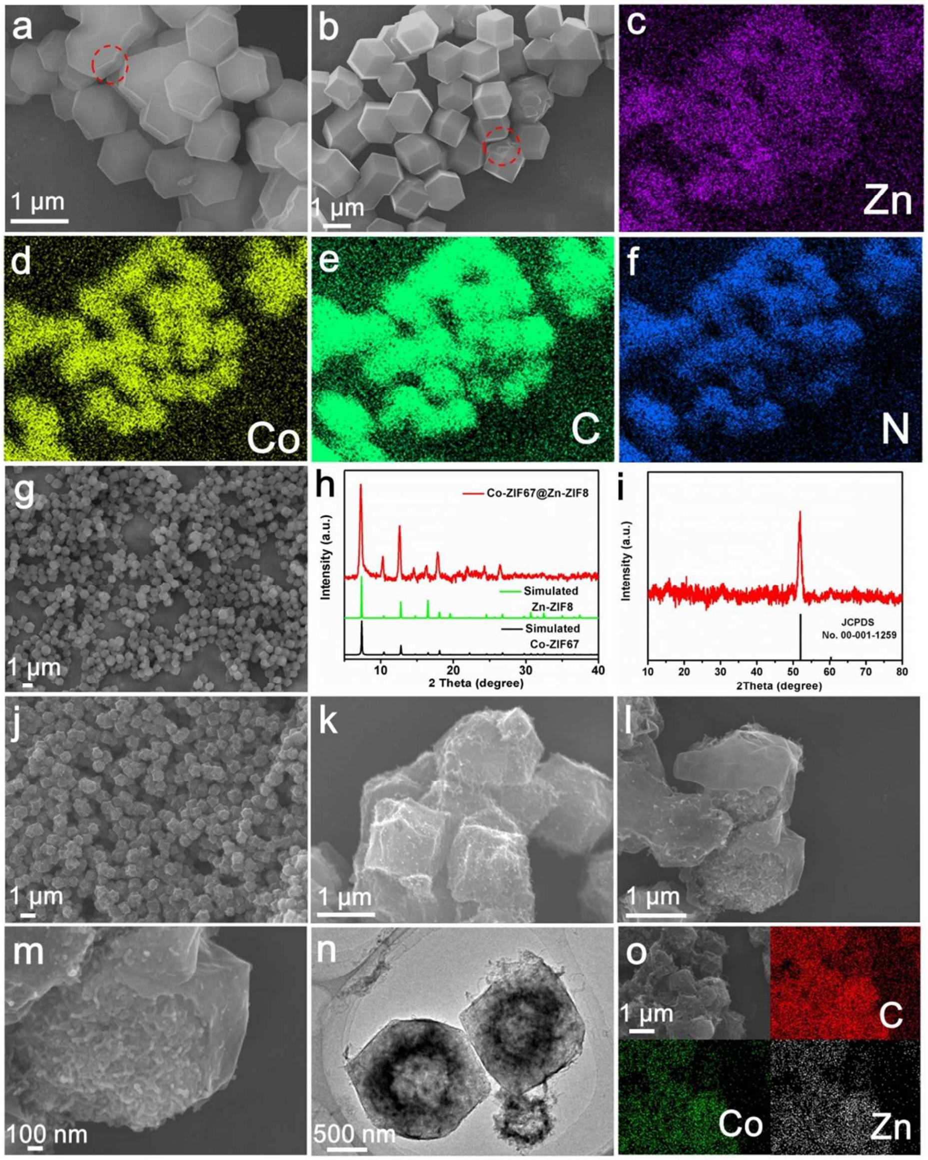

Figure S16. Characterizations of ZIF-67@ZIF8 precursor and derived CNT-assembled core-shell dodecahedra. (a, b, g) SEM image of ZIF-67@ZIF8 precursor. (c-f) Elemental mapping images of ZIF-67@ZIF8 precursor, including C, N, Co and Zn elements. (h) XRD pattern of ZIF-67@ZIF8 precursor. (i) XRD pattern of CNT-assembled core-shell dodecahedra. (j-m) SEM images of

CNT-assembled core-shell dodecahedra. (n) TEM image of CNT-assembled core-shell dodecahedra. (o) Elemental mapping image of CNT-assembled core-shell dodecahedra, including C, Co and Zn elements.

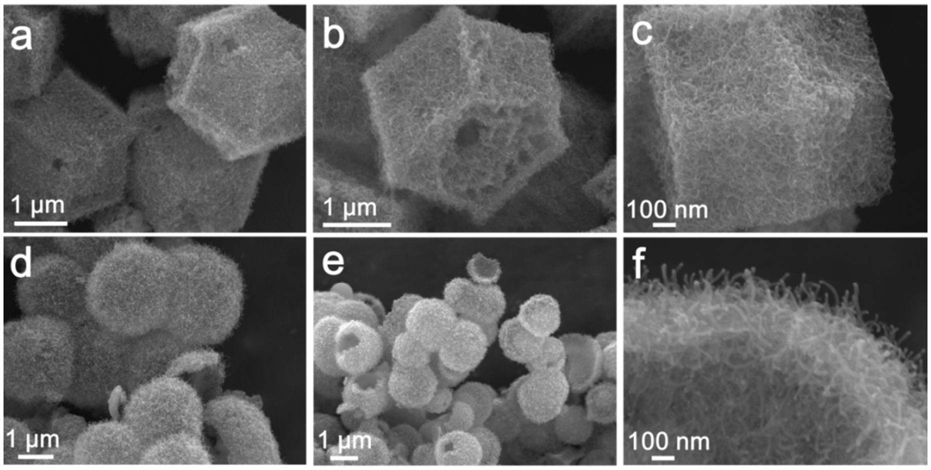

Figure S17. (a-c) SEM images of broken N-CNT-assembled hollow dodecahedra. (d-f) SEM images of broken CNT-assembled hollow microspheres.

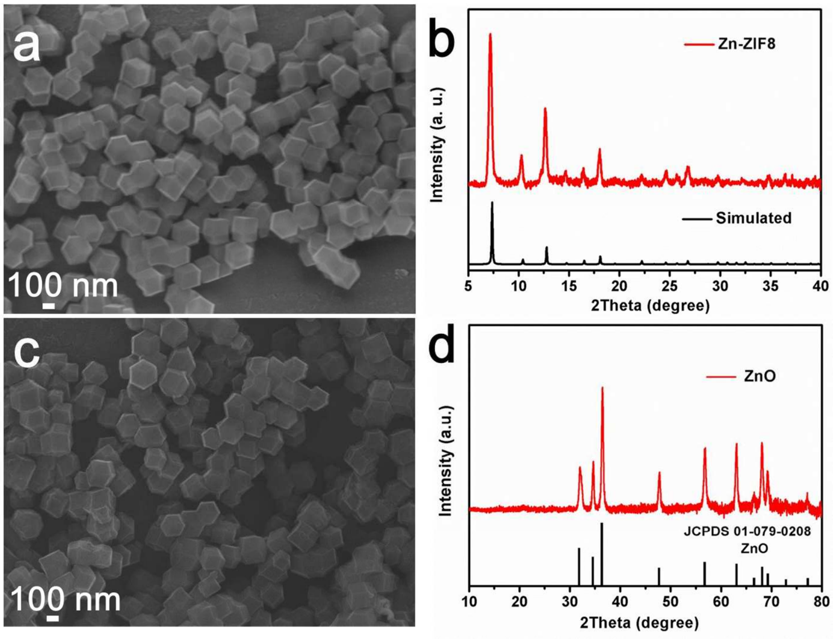

Figure S18. Characterizations of Zn-ZIF8 precursor and derived dodecahedra. (a, b) SEM image and XRD pattern of Zn-ZIF8 precursor, respectively. (c, d) SEM image and XRD pattern of derived dodecahedra, respectively.

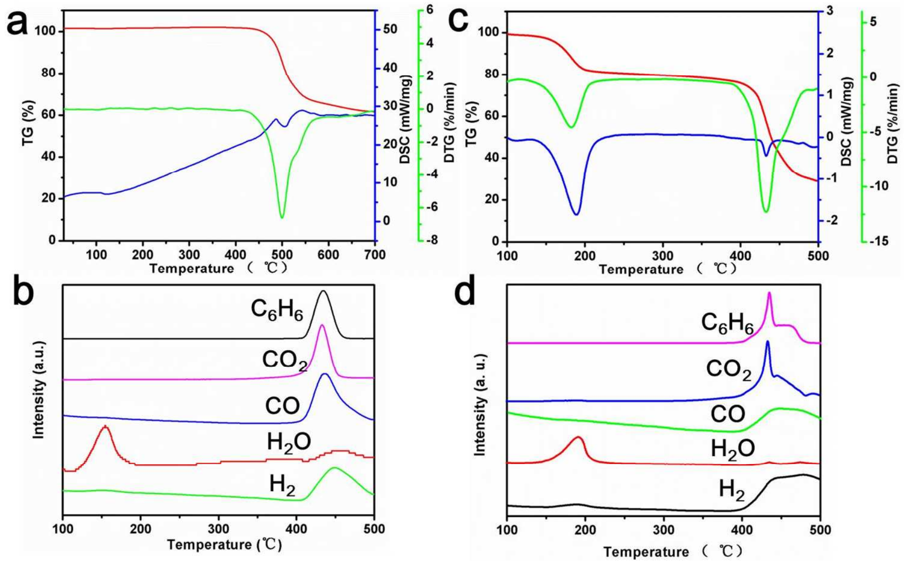

Figure S19. Characterizations of the pyrolysis process of Ni-BTC and Co-MOF precursors by TGA-MS technique. (a) TG, DSC and DTG curves of Ni-BTC precursor. (b) The corresponding MS curves of C_6H_6, H_2, CO_2, CO and H_2O, respectively. (c) TG, DSC and DTG curves of Co-MOF precursor. (d) The corresponding MS curves of C_6H_6, H_2, CO_2, CO and H_2O, respectively.

The pyrolysis processes of Ni-BTC and Co-MOF precursors were explored by TGA-MS technique, along with energy changes and gas release (Figure S19). For Ni-BTC precursors, the pyrolysis reaction occurred at about 450 °C. Due to the gas release, the corresponding mass loss was ~40 wt%. The released gases included C_6H_6, H_2, CO_2, CO and H_2O. For Co-MOF precursors, two stages of mass loss can be attributed to the solvent volatilization (< 200 °C, ~20 wt%), the gas release (>400 °C, ~45 wt%). The released gases included C_6H_6, H_2, CO_2, CO and H_2O.

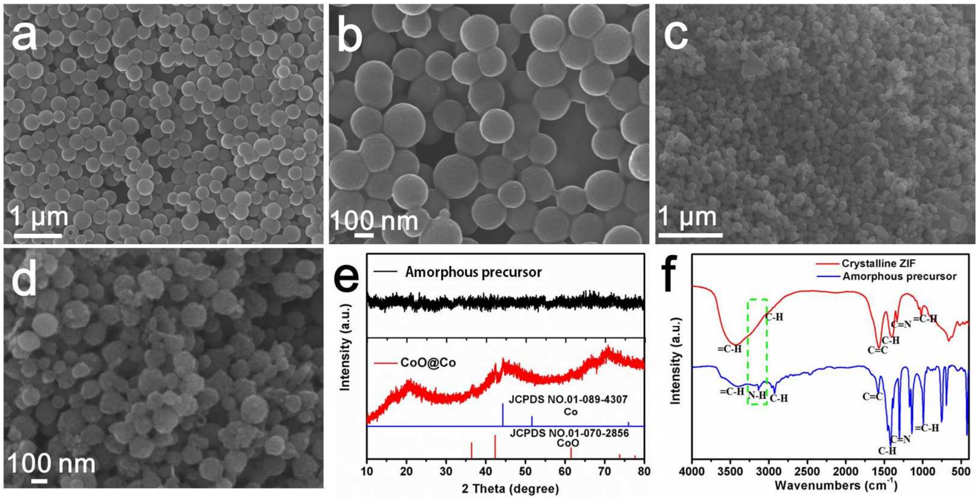

Figure S20. Characterizations of amorphous precursor and derived product. (a, b) SEM images of amorphous precursor. (c, d) SEM images of derived product after complete pyrolysis at 435 °C (2 °C min^{-1}) in argon for 8h. (e) XRD patterns of amorphous precursor and derived product. (f) FTIR spectra of amorphous precursor and crystalline ZIF.

On the basis of Fourier-Transform Infrared (FTIR) spectrum analysis, the N-H vibrations at around 3200 cm^{-1} indicates no obvious coordination between metal ions/clusters and organic ligands.

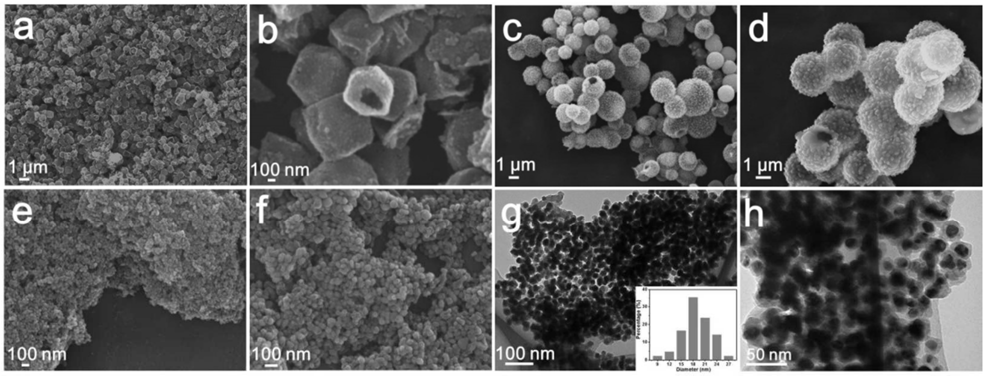

Figure S21. Characterizations of MOFs-derived structures after being treated at higher temperature. (a, b) SEM images of ZIF-67-derived nanoparticles-assembled dodecahedra after treated at 500 °C (2 °C min^{-1}) in argon for 8 h. (c, d) SEM images of Ni-BTC-derived nanoparticles-assembled hollow microspheres after treated at 500 °C (2 °C min^{-1}) in argon for 8 h. (e-h) SEM images and TEM images of Co-BTC-derived nanoparticles-assembled structures after treated at 500 °C (2 °C min^{-1}) in argon for 8 h. Inset of (g) is the diameter distribution of nanoparticles.

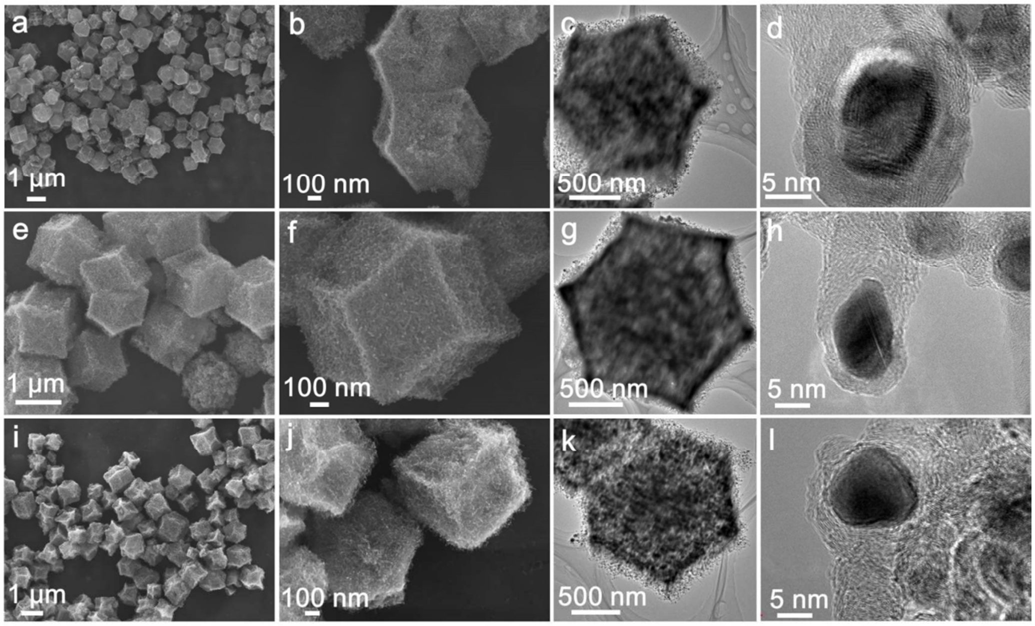

Figure S22. Morphology characterizations of N-CNTs-550, N-CNTs-650 and N-CNTs-750 samples. (a-d) SEM images and TEM images of N-CNTs-550 sample. (e-h) SEM images and TEM images of N-CNTs-650 sample. (i-l) SEM images and TEM images of N-CNTs-750 sample.

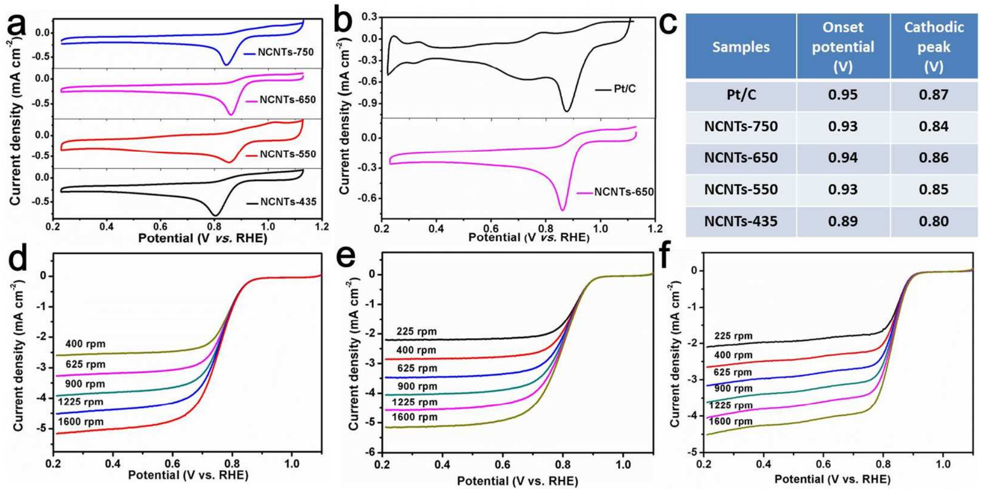

Samples	Onset potential (V)	Cathodic peak (V)
Pt/C	0.95	0.87
NCNTs-750	0.93	0.84
NCNTs-650	0.94	0.86
NCNTs-550	0.93	0.85
NCNTs-435	0.89	0.80

Figure S23. ORR electrocatalytic performances of N-CNTs. (a) CV curves of N-CNTs-435, N-CNTs-550, N-CNTs-650 and N-CNTs-750 samples. (b) CV curves of both N-CNTs-650 sample and Pt/C. (c) Contrastive analysis of the corresponding onset potentials and cathodic peaks. (d-f) LSV curves of N-CNTs-435, N-CNTs-550 and N-CNTs-750 samples in O_2-saturated 0.1 M KOH at a scan rate of 5 mV s^{-1} and different rotation rates.

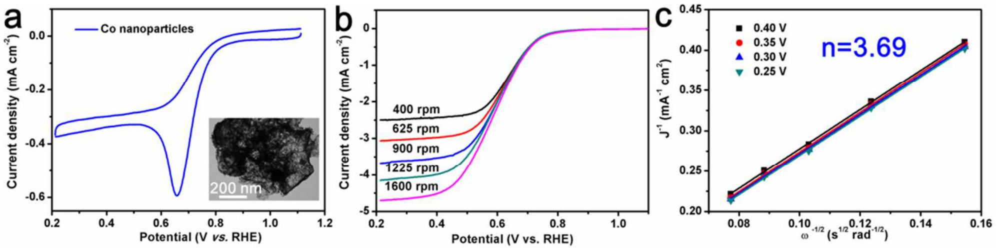

Figure S24. Characterizations and ORR electrocatalytic performances of bare Co nanoparticles. (a) CV curve at a scan rate of 5 mV s^{-1}, inset of (a) is the TEM image. (b) LSV curves in O_2-saturated 0.1 M KOH at a scan rate of 5 mV s^{-1} and different rotation rates. (c) K-L plots at different potentials.

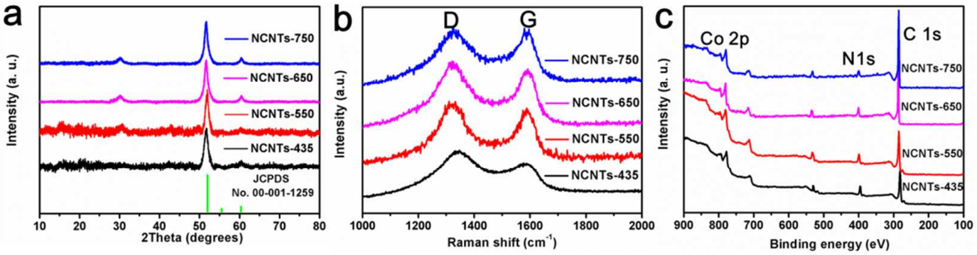

Figure S25. Structural characterizations of N-CNTs-435, N-CNTs-550, N-CNTs-650 and N-CNTs-750 samples. (a) XRD patterns. (b) Raman spectra. (c) XPS spectra.

We further used XRD and Raman spectroscopy to investigate the crystalline structure and graphitization degree of these samples. XRD patterns detected by Co Kα radiation source reveal that an obvious peak at ~30° attributed to graphitic carbon (200) appears in N-CNTs-550, N-CNTs-650, and N-CNTs-750 samples, indicating high graphitization. The obvious peaks at ~52° and ~60° in all samples are attributed to Co (111) and Co (200). Raman spectra show that the I_D/I_G band intensity ratios of these samples are 1.22, 1.10, 1.03 and 1.02, respectively. XPS spectra of these samples further confirm the presence and distribution of Co, C and N.

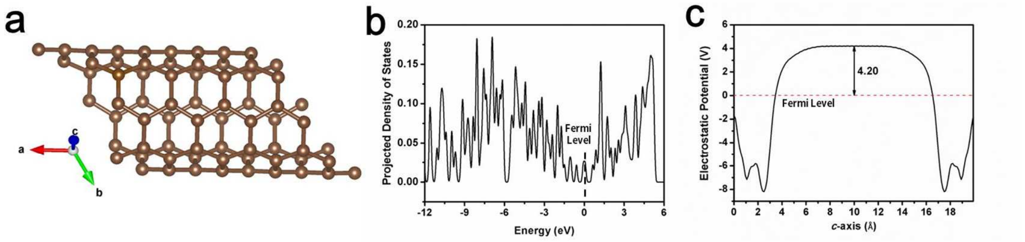

Figure S26. DFT simulation results of pure single-walled CNTs. (a) The structure model of single-walled CNTs. (b) Projected DOS of single-walled CNTs. (c) Calculated electrostatic potential profile averaged on the plane perpendicular to the c-axis as a function of the b-axis of pure CNTs. The Fermi level is aligned at 0 eV.

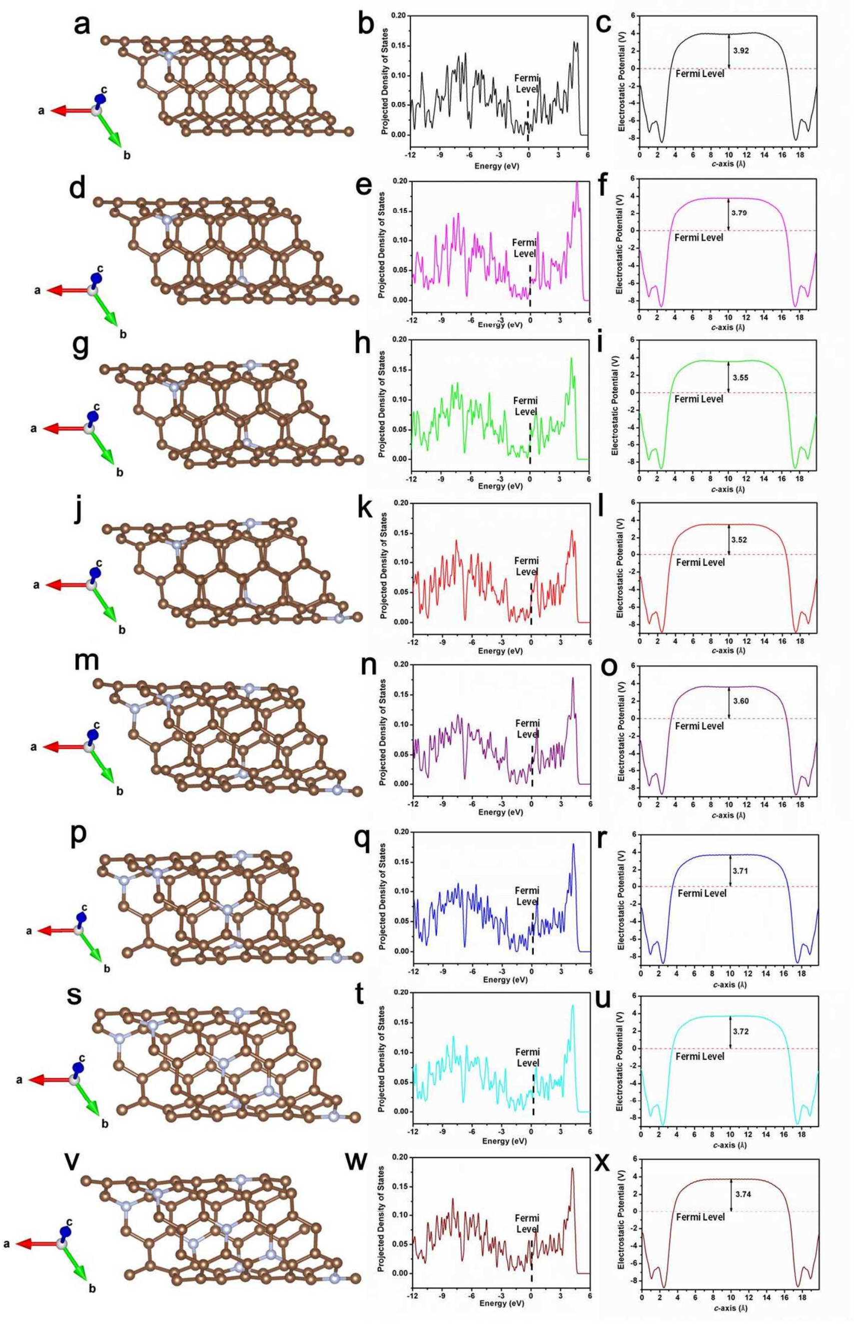

Figure S27. DFT simulation results of graphitic N-CNTs with various N contents. (a-c) The structure model, projected DOS and calculated electrostatic potential profile averaged on the plane perpendicular to the c-axis as a function of the b-axis of graphitic N-CNTs with 1.56% N content. (d-f) The structure model, projected DOS and corresponding calculated electrostatic potential profile of graphitic N-CNTs with 3.13% N content. (g-i) The structure model, projected DOS and corresponding calculated electrostatic potential profile of graphitic N-CNTs with 4.69% N content. (j-l) The structure model, projected DOS and corresponding calculated electrostatic potential profile of graphitic N-CNTs with 6.25% N content. (M-O) The structure model, projected DOS and corresponding calculated electrostatic potential profile of graphitic N-CNTs with 7.81% N content. (p-r) The structure model, projected DOS and corresponding calculated electrostatic potential profile of graphitic N-CNTs with 9.38% N content. (s-u) The structure model, projected DOS and corresponding calculated electrostatic potential profile of graphitic N-CNTs with 10.94% N content. (v-x) The structure model, projected DOS and corresponding calculated electrostatic potential profile of graphitic N-CNTs with 12.5% N content. The Fermi level is aligned at 0 eV.

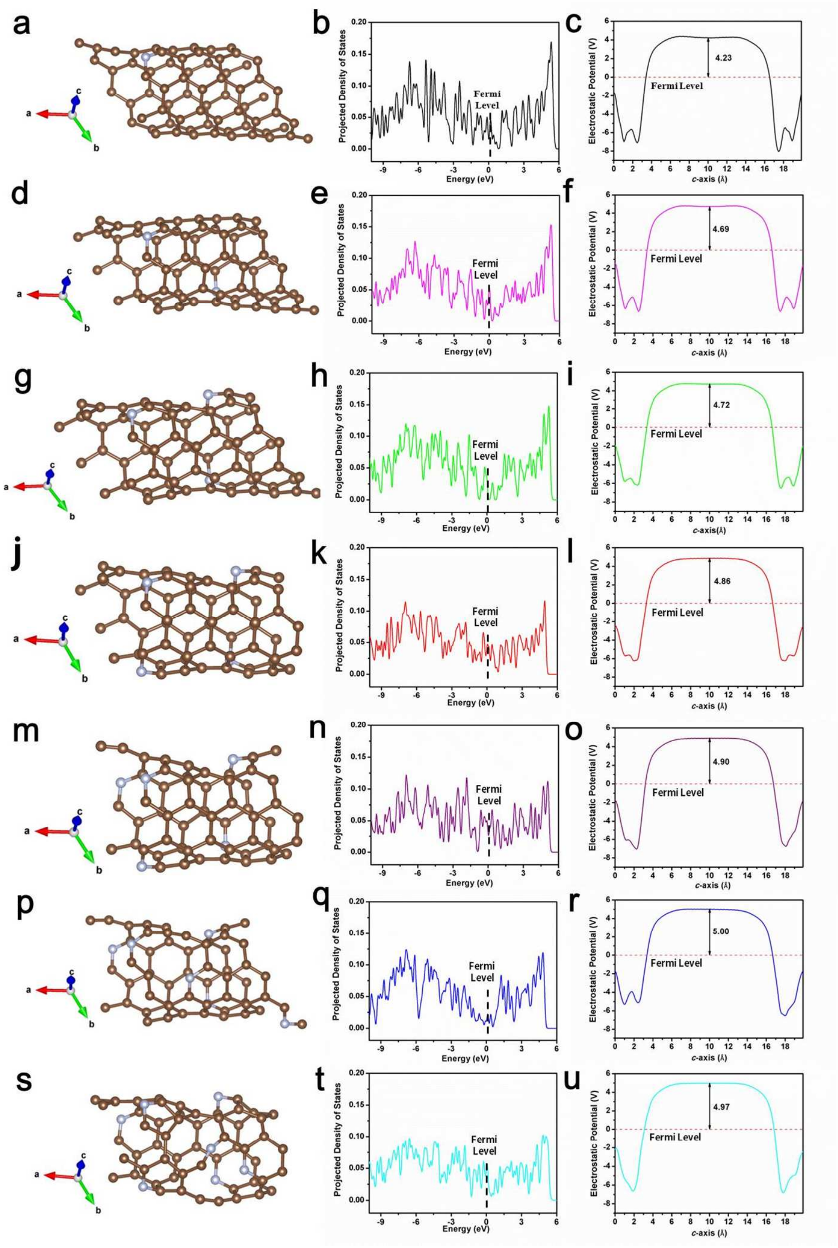

Figure S28. DFT simulation results of pyridinic N-CNTs with various N contents. (a-c) The structure model, projected DOS and calculated electrostatic potential profile averaged on the plane perpendicular to the c-axis as a function of the b-axis of pyridinic N-CNTs with 1.59% N content. (d-f) The structure model, projected DOS and corresponding calculated electrostatic potential profile of pyridinic N-CNTs with 3.33% N content. (g-i) The structure model, projected DOS and corresponding calculated electrostatic potential profile of pyridinic N-CNTs with 4.92% N content. (j-l) The structure model, projected DOS and corresponding calculated electrostatic potential profile of pyridinic N-CNTs with 6.67% N content. (m-o) The structure model, projected DOS and corresponding calculated electrostatic potential profile of pyridinic N-CNTs with 8.47% N content. (p-r) The structure model, projected DOS and corresponding calculated electrostatic potential profile of pyridinic N-CNTs with 10.34% N content. (s-u) The structure model, projected DOS and corresponding calculated electrostatic potential profile of pyridinic N-CNTs with 12.28% N content. The Fermi level is aligned at 0 eV.

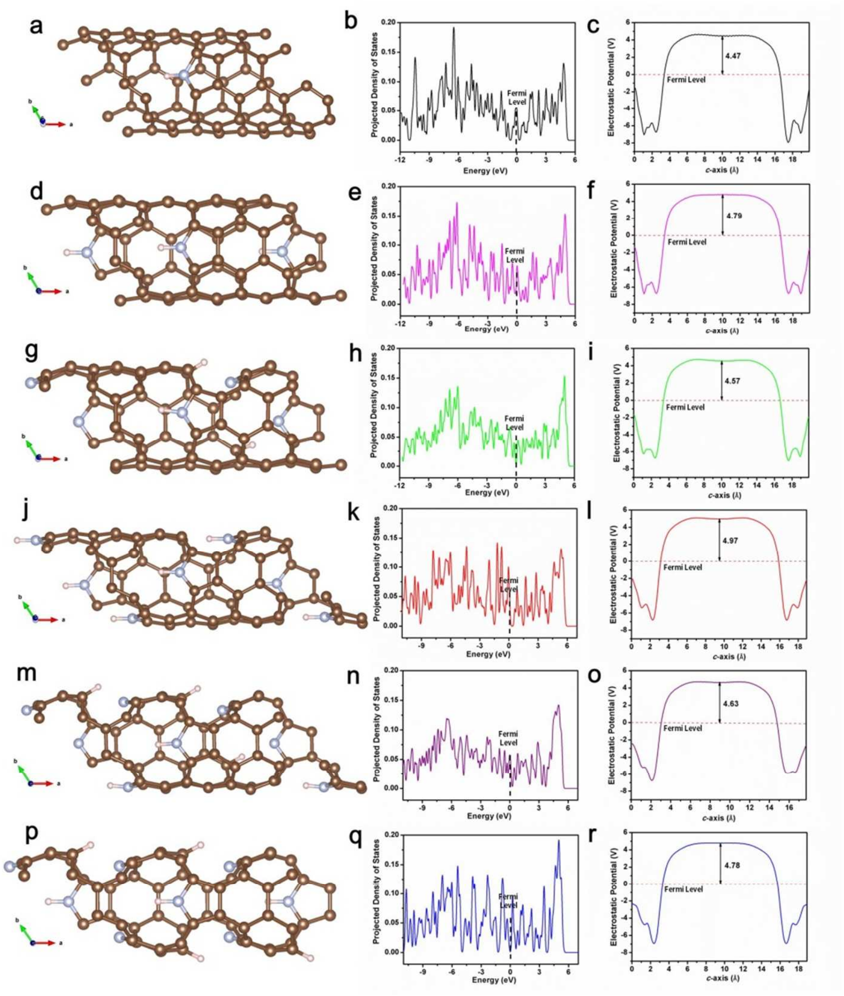

Figure S29. DFT simulation results of pyrrolic N-CNTs with various N contents. (a-c) The structure model, projected DOS and calculated electrostatic potential profile averaged on the plane perpendicular to the c-axis as a function of the b-axis of pyrrolic N-CNTs with 1.59% N content. (d-f) The structure model, projected DOS and corresponding calculated electrostatic potential profile of pyrrolic N-CNTs with 3.33% N content. (g-i) The structure model, projected DOS and corresponding calculated electrostatic potential profile of pyrrolic N-CNTs with 4.92% N content. (j-l) The structure model, projected DOS and corresponding calculated electrostatic potential profile of pyrrolic N-CNTs with 6.67% N content. (m-o) The structure model, projected DOS and corresponding calculated electrostatic potential profile of pyrrolic N-CNTs with 8.47% N content. (p-r) The structure model, projected DOS and corresponding calculated electrostatic potential profile of pyrrolic N-CNTs with 10.34% N content. The Fermi level is aligned at 0 eV.

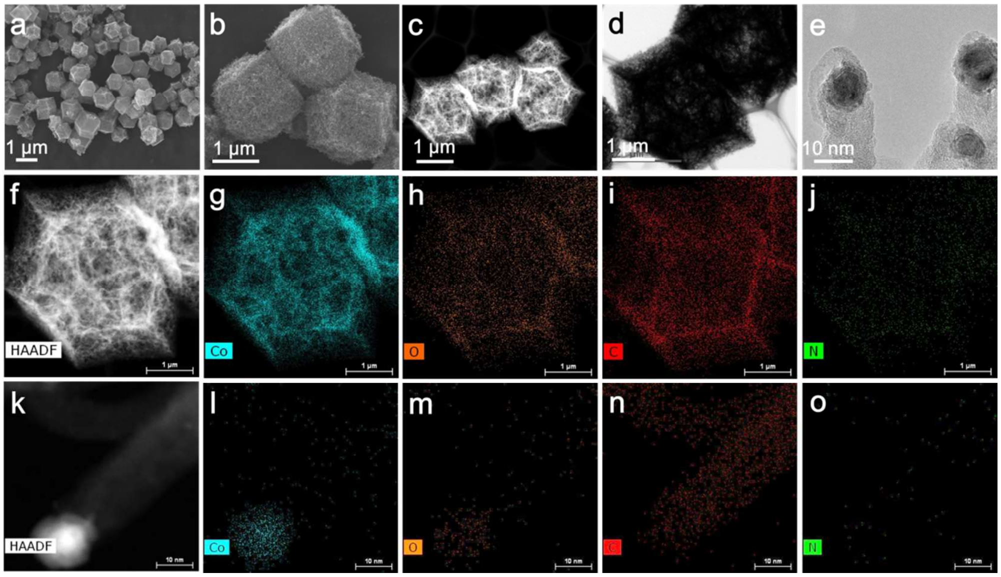

Figure S30. Morphology characterizations of Co_3O_4@N-CNTs sample. (a, b) SEM image. (c) STEM-HAADF image. (d) TEM image. (e) HRTEM image. (f-j) STEM-EDS mappings on the dodecahedra for Co, O, C, O and N. (k-o) STEM-EDS mappings on the carbon nanotubes for Co, O, C, O and N.

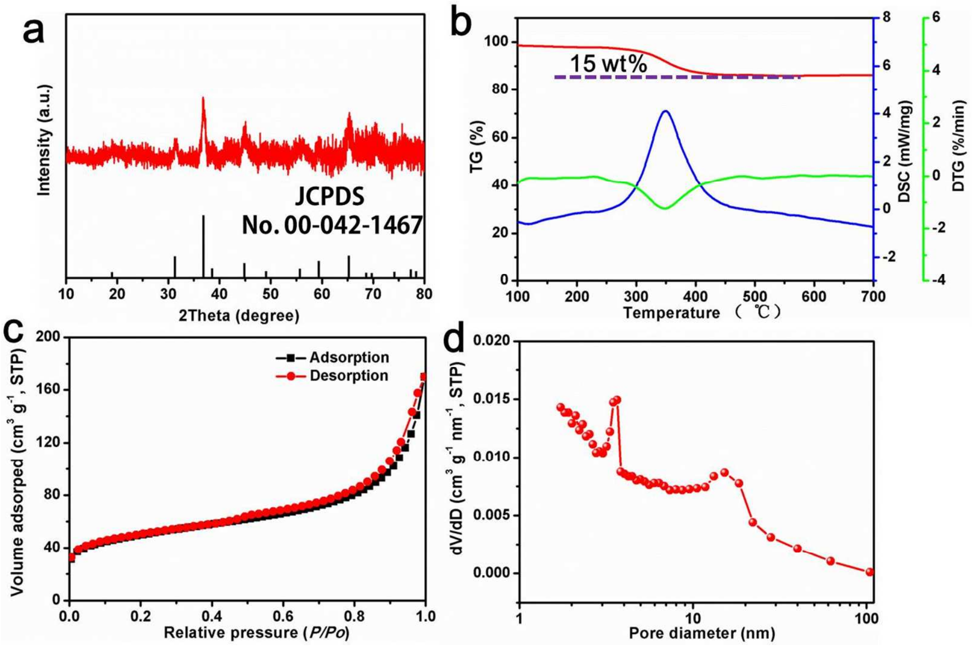

Figure S31. Structure characterizations of Co_3O_4@N-CNTs sample. (a) XRD pattern. (b) TG-DTG-DSC curves. (c) N_2 adsorption-desorption isotherms. (d) The pore size distribution.

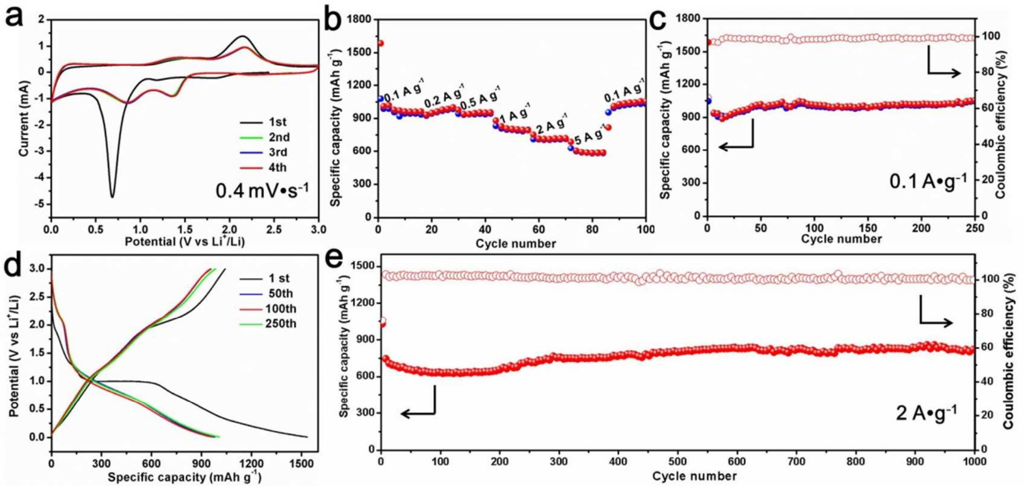

Figure S32. Electrochemical performances of Co_3O_4 nanoparticles encapsulated into N-CNTs in LIBs. (a) First four CV curves tested at a scan rate of 0.4 mV·s^{-1} in the potential range from 0.01 to 3.0 V versus Li^+/Li. (b) Rate performance tested at current densities of 0.1, 0.2, 0.5, 1, 2 and 5 A·g^{-1}. (c) Cycling performance and Coulombic efficiency tested at a current density of 0.1 A·g^{-1}. (d) The corresponding charge-discharge voltage profiles at different cycles. (e) Cycling performance and Coulombic efficiency tested at a high current density of 2 A·g^{-1}.

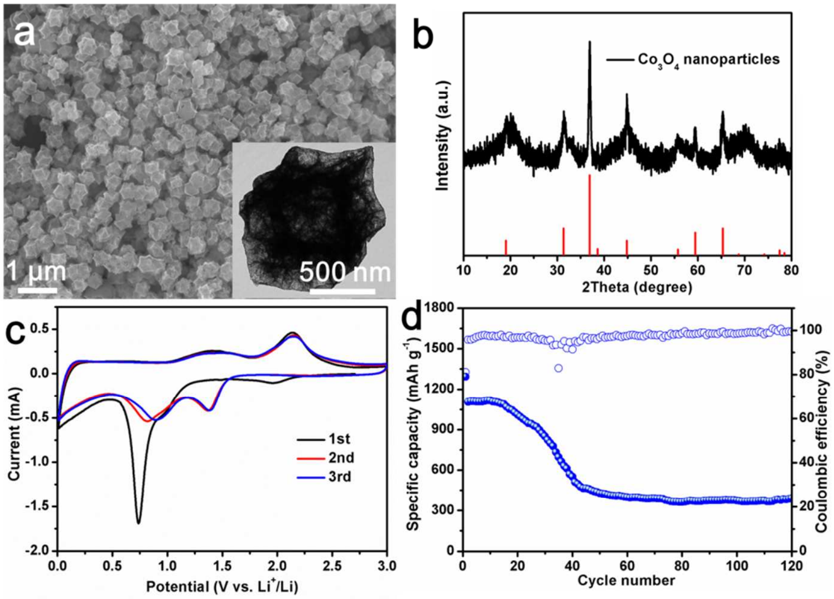

Figure S33. Characterizations and lithium storage performances of bare Co_3O_4 nanoparticles. (a) SEM image, inset of (a) is the TEM image. (b) XRD pattern. (c) CV curve at a scan rate of 0.4 mV s-1 in the voltage range of 0.01-3.0 V. (d) Cycling performance and Coulombic efficiency tested at a current density of 0.1 A·g^{-1}.

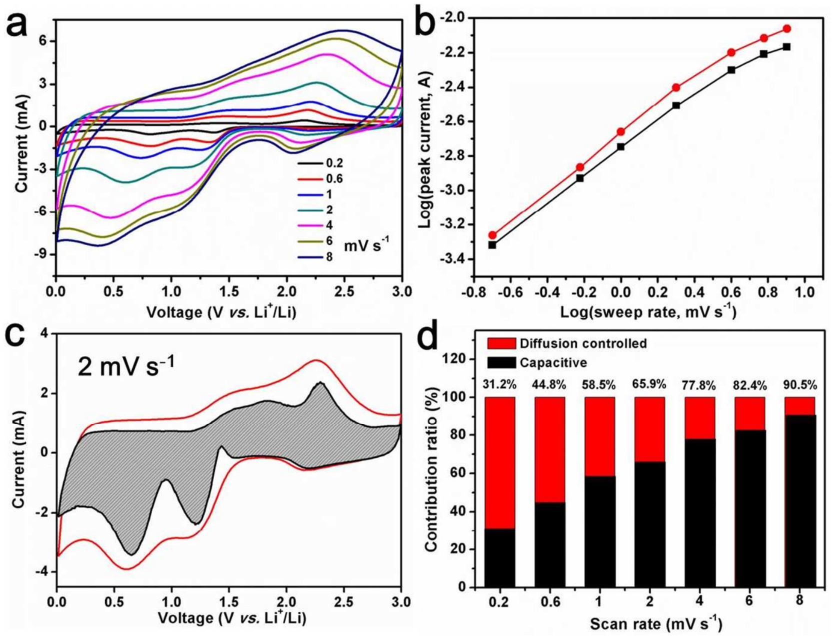

Figure S34. Kinetics analysis of the electrochemical behavior towards Li$^+$ for Co_3O_4@N-CNTs electrode. (a) CV curves at various scan rates ranging from 0.2 to 8 mV·s^{-1}. (b) Determination of the b-value using the relationship between peak current and scan rate. (c) Separation of the capacitive and diffusion currents at a scan rate of 2 mV·s^{-1}. (d) Contribution ratio of the capacitive and diffusion-controlled charge versus scan rate.

To explain the excellent performance of Co_3O_4@N-CNTs, CV analysis is firstly carried out to gain further insight into the electrochemical kinetics of electrode materials. The CV curves at different scan rates from 0.2 to 8 mV·s^{-1} were performed. According to the relationship between the measured current (i) and the scan rate (v): $i=av^b$. (*Nat. Commun.* **2015**, *6*, 6929.) Particularly, the b-value of 0.5 indicates total diffusion controlled behavior, and 1.0 represents a capacitive process. The b-value of ~0.8 for both selected peaks can be quantified at scan rates from 0.2 to 8 mV·s^{-1}, suggesting the kinetics of both capacitive and diffusion-controlled characteristics. The 65.9 % of the total capacity is capacitive at a scan rate of 2 mV·s^{-1}. Contribution ratios between the two different processes at different scan rates show that the ratio of capacitive capacity gradually improves with the scan rate increasing, enabling high rate capability.

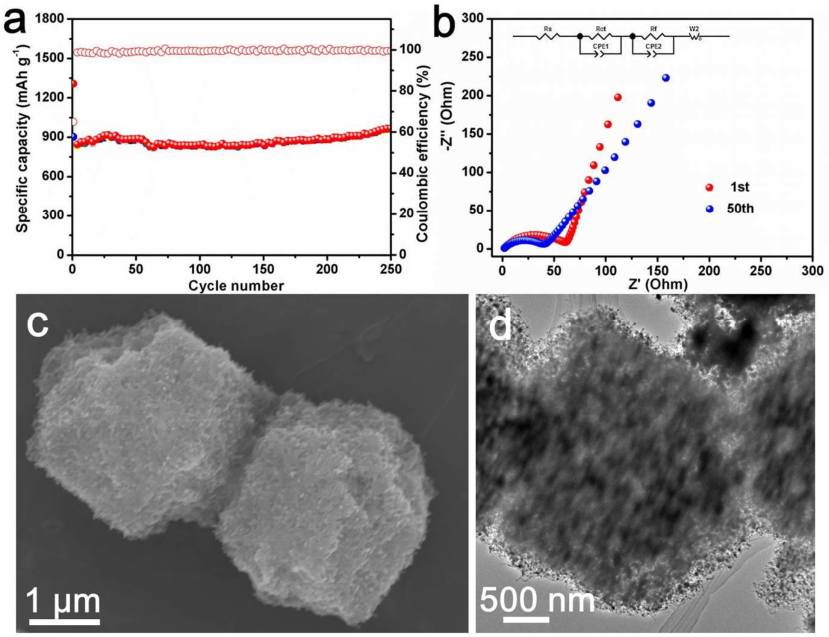

Figure S35. Electrochemical performances and morphology characterizations after cycling of Co_3O_4@N-CNTs electrode in LIBs. (a) Cycling performance and Coulombic efficiency tested at current density of 0.5 A g^{-1}. (b) The Nyquist plots at the 1st and 50th cycles, respectively. (c, d) SEM image and TEM image after 250 cycles at 0.5 A·g^{-1}.

At a current density of 0.5 A·g^{-1}, the Co_3O_4@N-CNTs can still keep stable after 250 cycles with capacity retention of over 100%, showing excellent electrochemical stability. In addition, electrochemical impedance spectrum (EIS) was measured. The charge transfer resistance (Rct) of Co_3O_4@N-CNTs is 69 Ω, and after cycling 50 times, the value of Rct decreases to 40 Ω, suggesting their fast electronic mobility. Furthermore, the morphology of electrode can remain integrated after 250 cycles at a current density of 0.1 A·g^{-1}, showing great structural stability.

Table S1. Elemental analysis of ZIF-67, N-CNTs-435, N-CNTs-550, N-CNTs-650 and N-CNTs-750 based on CHNS and ICP results.

Materials	**C (wt%)**	**N (wt%)**	**H (wt%)**	**Co (wt%)**
ZIF-67	40.76	24.89	4.37	29.98
N-CNTs-435	40.88	14.81	2.32	41.99
N-CNTs-550	41.35	8.67	1.18	48.80
N-CNTs-650	42.80	5.05	0.45	51.70
N-CNTs-750	44.60	2.31	0.23	52.86

Table S2. A summary of synthetic methods for high-quality CNTs.

Methods	**Types of high-quality CNTs**	**Carbon sources**	**Advantages**	**Disadvantages**	**References**
Bottom-up organic synthesis	Chiral CNTs	Organic molecules	● Precise control	■ Low yield ■ Complex synthetic process ■ High cost	*Acc. Chem. Res.* **2012**, *45*, 1378-1389.
Tradition solid-phase reaction	N-doped CNTs	Melamine	● Simple method ● Easy control	■ Chaotic stacking ■ High temperature	*J. Mater. Chem. A* **2013**, *1*, 3302-3308.

Chemical vapor deposition	CNT arrays Organized CNTs	Gases	● Easy control ● Simple method ● Relative high yield	■ High temperature ■ Relative high cost ■ Substrate modification	*Nature* **2002**, *416*, 495-496; *Science* **2009**, *323*, 760-764.
Low-temperature oriented formation	CNTs-assembled structures	MOFs	● Low temperature ● High yield ● Controlled assembled structures ● Simple method	_____	Our work

Table S3. A summary of various electrocatalysts for ORR.

Electrocatalysts	**Onset potential (V)**	**Half-wave potential (V)**	**CV peak potential (V)**	**n**	**References**
N-CNTs-650	0.94	0.85	0.87	3.94	Our work
Co_3O_4/N-rmGO	0.88	0.79	0.83	3.9	*Nat. Mater.* **2011***, 10,* 780-786.
Hydrogenated-MnO_2 nanorods	0.9	0.76	0.77	3.2	*Adv. Energy Mater.* **2015***, 5,* 1400654.
Carbon nanotube frameworks	0.97	0.87	0.87	3.97	*Nat. Energy* **2016**, *1*, 15006.
Porous carbon/graphene	0.95	0.82	0.82	3.98	*Angew. Chem. Int. Ed.* **2014**, *53*, 14235-14239.
Fe-N-CNFs	0.93	0.82	0.82	3.93	*Angew. Chem. Int. Ed.*

					2015, *54*, 8179-8183.
$CoMn_2O_4$ nanotubes	0.89	0.72	0.81	3.6	*Nano Res.* **2016**, *9*, 2445-2457.
PANI-Fe-C	0.91	0.81	N/A	4	*Science* **2011**, *332*, 443-447.
Mesoporous N-doped carbon	0.97	0.85	0.83	3.97	*Nat. Commun.* **2014**, *5*, 5974.
Fe-N/C-800	0.92	0.80	0.85	3.96	*J. Am. Chem. Soc.* **2014**, *136*, 11027-11033.
CNT/graphene hybrid	0.89	0.76	0.75	4	*Nat. Nanotech.* **2012**, *7*, 394-400.

Table S4. Comparisons of our work and previous reports on different nanostructured Co_3O_4 for LIBs.

Morphology	**Voltage range (V)**	**Current density (mA g^{-1})**	**Cycle number**	**Residual capacity (mAh g^{-1})**	**Capacity retention**	**Reference**
Co_3O_4@N-CNTs	0.01-3	100 500 2000	250 250 1000	1030 905 752	110% 108% ~100%	Our work
Porous Co_3O_4 hollow dodecahedra	0.01-3	100	100	780	79%	*Small* **2014**, *10*, 1932-1938.
Co_3O_4/NPC hybrid	0.01-2.5	100	100	892	68%	*Nano Energy* **2015**, *12*, 1-8.
Co_3O_4/Graphene composite	0.01-3	50	30	935	116%	*ACS nano* **2010**, *4*, 3187-3194.
Mesoporous peapod-like Co_3O_4@CNTs	0.01-3	100	100	700	81%	*Angew. Chem. Int. Ed.* **2015**, *54*, 7060-7064.

Multishelled Co_3O_4 hollow microspheres	0.05-3	50	30	1615	104%	*Angew. Chem. Int. Ed.* **2013**, *52*, 6417-6420.
Carbon-doped Co_3O_4 hollow nanofibers	0.01-3	200	100	1121	93%	*Adv. Funct. Mater.* **2016**, *26*, 1428-1436.
Hierarchical CNT/Co_3O_4 microtubes	0.01-3	1000	200	750	98%	*Angew. Chem. Int. Ed.* **2016**, *55*, 5990-5993.
MWCNTs/Co_3O_4	0.01-3	100	100	813	94%	*ACS nano* **2015**, *9*, 1592-1599.
Hollow structured Co_3O_4 Nanoparticles	0.01-3	50	50	880	97%	*ACS nano* **2015**, *9*, 1775-1781.